Ou *et al. Energy Mater.* **2025**, *5*, 500088
DOI: 10.20517/energymater.2024.277

Energy Materials

Article

Open Access

Check for updates

Boosting the ionic conductivity of amorphous oxychloride solid electrolytes via different degrees of amorphization

Junquan Ou[1], Ishani Senevirathna[2], Vignyatha Tatagari[1], Adil Saleem[1], Carlo Segre[2], Leon Shaw[1,*]

[1]Department of Mechanical, Materials and Aerospace Engineering, Illinois Institute of Technology, Chicago, IL 60616, USA.
[2]Department of Physics, Illinois Institute of Technology, Chicago, IL 60616, USA.

[*]**Correspondence to:** Prof. Leon Shaw, Department of Mechanical, Materials and Aerospace Engineering, Armour College of Engineering, 10 W. 32nd Street, Chicago, IL 60616, USA. E-mail: lshaw2@iit.edu

How to cite this article: Ou, J.; Senevirathna, I.; Tatagari, V.; Saleem, A.; Segre, C.; Shaw, L. Boosting the ionic conductivity of amorphous oxychloride solid electrolytes via different degrees of amorphization. *Energy Mater.* **2025**, *5*, 500088. https://dx.doi.org/10.20517/energymater.2024.277

Received: 5 Dec 2024 **First Decision:** 3 Jan 2025 **Revised:** 15 Feb 2025 **Accepted:** 25 Feb 2025 **Published:** 22 Apr 2025

Academic Editors: Hong Xu, Jinping Liu **Copy Editor:** Ping Zhang **Production Editor:** Ping Zhang

Abstract

Solid electrolytes provide improved safety, greater electrochemical and thermal stability, and better compatibility with high-energy materials than liquid electrolytes. Compared to crystalline solid electrolytes, amorphous solid electrolytes offer reduced grain boundary resistance, enhanced processability, isotropic ionic conductivity and superior mechanical properties. Herein, the impacts of varying high-energy ball milling intensities on the degree of amorphization of amorphous $1.6Li_2O$-$TaCl_5$ oxychloride and thus its ionic conductivity are investigated. It is shown that the ionic conductivity of amorphous $1.6Li_2O$-$TaCl_5$ can reach as high as 8.30×10^{-3} S/cm at room temperature by increasing the degree of amorphization. Furthermore, the sample exhibiting the highest ionic conductivity also releases the largest stored enthalpy upon heating, indicating that structural defects in amorphous $1.6Li_2O$-$TaCl_5$ materials play a crucial role in enhancing their Li-ion conductivities. This discovery opens the door for boosting the ionic conductivities of other amorphous electrolytes in the future by increasing the degree of amorphization.

Keywords: Solid electrolyte, Li-ion batteries, solid-state batteries, Li-ion conductivity, amorphous phase

INTRODUCTION

Lithium-ion batteries (LIBs) have become indispensable in modern energy storage systems. Using solid-

© The Author(s) 2025. **Open Access** This article is licensed under a Creative Commons Attribution 4.0 International License (https://creativecommons.org/licenses/by/4.0/), which permits unrestricted use, sharing, adaptation, distribution and reproduction in any medium or format, for any purpose, even commercially, as long as you give appropriate credit to the original author(s) and the source, provide a link to the Creative Commons license, and indicate if changes were made.

state electrolytes (SSEs) instead of organic liquid electrolytes is expected to solve the safety risk caused by the flammability of liquid electrolytes faced by LIBs[1]. SSEs also have the potential to widen the electrochemical windows and improve the energy densities of rechargeable batteries[2]. A wide range of SSEs have been developed and studied, including sulfide, oxide, halide, oxyhalide, phosphate, and polymer SEs. Specifically, sulfide-based SSEs, such as Li-argyrodite[3,4] and lithium germanium phosphorus sulfide (LGPS) type materials[5,6] (e.g., $Li_{10}GeP_2S_{12}$), have the advantage of high ionic conductivity and easy processing, but suffer from the high moisture sensitivity and narrow electrochemical window. Some oxide-based SSEs, such as garnet-type materials[7,8], have excellent chemical and thermal stability and wide electrochemical windows. However, their brittle and rigid structures lead to poor interfacial compatibility, resulting in lower interfacial ionic conductivity. Other oxide-based SSEs including perovskite[7,8] ($Li_{3x}La_{2/3-x}TiO_3$) and thio-LISICON (lithium superionic conductor)[9,10] SSEs suffer from insufficient electrochemical stability, especially at the lower potential side. Halide-based SSEs, exemplified by the Li-M-Cl system (M=Y, In, Sc, Zr)[11,12], offer a unique combination of aqueous synthesis routes (enabling cost-effective scale-up), high ionic conductivity, and wide operational voltage ranges. Recent advances in doping strategies, such as Ca^{2+} substitution in Li_2ZrCl_6, further enhance their compatibility with high-voltage cathodes while retaining competitive ionic transport[13]. Nevertheless, their intrinsic instability against lithium metal anodes remains a critical barrier. Oxychloride-based (Li_3OCl)[14,15] and lithium-metal-oxychloride SSEs ($LiMOCl_4$)[16] exhibit higher ionic conductivities than halide-based SSEs but their instability to moisture is an inevitable defect. Phosphorous-based SSEs (LiPON) are the earliest successfully developed inorganic SSE in the early 1990s[17,18]. Although LiPON provides superb interfacial compatibility with lithium metal anode, an intrinsic shortcoming is its too low ionic conductivity (10^{-6} S/cm) at room temperature (RT), which greatly hinders further application. Fluorinated lithium-rich anti-perovskite (F-LiRAP) SSEs have been explored through engineering Frenkel defects to enhance lithium-ion transport. By introducing lithium-rich and lithium-vacancy couples via fluoride incorporation, the ionic conductivity of F-LiRAP reaches 1.1×10^{-6} S/cm at 25 °C[19]. However, this conductivity remains similar to that of LiPON, indicating challenges in achieving higher conductivity for practical applications. On the other hand, polymer-based SSEs demonstrate excellent interfacial contact and good processability, making them highly promising candidates for practical applications[20-23]. However, they suffer from insufficient mechanical strength and an inadequate electrochemical stability window, rendering them unsuitable for use in high-voltage lithium batteries.

Compared with crystalline SSEs, amorphous SSEs lack long-range order and present the primary advantages of softness, easy fabrication, low grain boundaries and wide composition variations[24-27]. Furthermore, the lack of long-range order in the amorphous structure results in more flexible and isotropic ionic pathways, reducing constraints on ion movement. The irregular potential energy landscape in amorphous materials leads to lower and fewer energy barriers, allowing ions to move more freely with less resistance[24-27]. Amorphous SSEs can be synthesized using various methods, including high-energy ball milling, melt-quenching, physical and chemical vapor deposition, irradiation, large supercooling of pure melt, hydrothermal reaction, and so on[28]. Among these methods, high-energy ball milling stands out as a cost-effective method while offering flexible control over material properties, including particle size, degree of amorphization, and homogeneity. An interesting phenomenon is that many simple lithium salts can be glassified by $TaCl_5$, resulting in a series of amorphous super lithium-ion conductors with high ionic conductivities (10^{-3} S/cm at RT)[29,30]. Furthermore, amorphous SSEs can also be formed from lithium-metal-oxychlorides with compositions of xLi_2O-MCl_y (M=Ta or Hf, $0.8 \leq x \leq 2$, $y = 5$ or 4) through high-energy ball milling with high ionic conductivity (6.6×10^{-3} S/cm at 25 °C) and oxidation resistance beyond 4 V *vs.* Li^+/Li[31]. It is reported that this group of SSEs has high ionic conductivity because (i) disordered and irregular $[TaCl_{5-a}O_a]^{a-}$ ($1 \leq a < 5$) arrangements in amorphous xLi_2O-MCl_y lead to abundant Li-Cl interactions and distorted Li-Cl sublattices, (ii) corner-shared oxygen (O-2Ta) networks induce a wide

range of distortions in Li sites, resulting in low Li-ion migration energy, and (iii) the unsaturated Ta-Cl…Li bond in $[TaCl_{5-a}O_a]^{a-}$ ($1 \leq a < 5$) has weak Coulombic forces between Li and Cl ions, making it easier for Li ions to jump from one site to another[31]. The composition of $1.6Li_2O$-$TaCl_5$ (LOTC) has been reported to have the best ionic conductivity of 6.6×10^{-3} S/cm at 25 °C among this group of materials[31].

In this study, we investigate whether the ionic conductivity of amorphous LOTC oxychloride can be further improved over 6.6×10^{-3} S/cm at 25 °C reported previously[31] via control in the degree of amorphization. By altering the intensity of high-energy ball milling, it is demonstrated that an ionic conductivity of 8.3×10^{-3} S/cm at RT, which is 25% higher than the highest ionic conductivity reported previously[31], can be achieved. Furthermore, differential scanning calorimetry (DSC) analysis reveals that the sample with the highest ionic conductivity releases the highest stored enthalpy upon heating, suggesting that structural defects in amorphous LOTC samples are an important factor for boosting their Li-ion conductivities. This discovery points to a new direction for boosting the ionic conductivities of many other amorphous SSEs by increasing the degree of amorphization in the future.

EXPERIMENTAL

Material synthesis

Amorphous LOTC oxychloride powder was synthesized via high-energy ball milling using SPEX mills with the starting materials Li_2O (purity > 97%, Sigma) and $TaCl_5$ (purity > 99.99%, Oakwood Chemical). The degree of amorphization was controlled through the ball milling intensity by changing the ball milling time or the density of balls. A typical synthesis consisted of 1 g of Li_2O + $TaCl_5$ mixture (mixed in a 1.6-to-1.0 molar ratio) and 20 g of stainless steel (SS) balls of 5 mm in diameter, leading to a ball-to-powder ratio of 20 to 1 (w/w). The powder mixture and steel balls were loaded in a SPEX mill canister inside an Ar-filled glovebox and sealed completely before being taken out for ball milling. Samples with different ball milling times are summarized in Table 1. To alter the ball milling intensity in addition to just changing the ball milling time, LOTC powder samples were also ball milled using ZrO_2 balls of 5 mm in diameter with the ball-to-powder ratio being 40 to 1 (w/w). To avoid significant temperature rise of the canister during ball milling, all ball milling was stopped after 1 h and rested for 30 min before continuing for another 1-h, 30-min, or 15-min ball milling, depending on the sample condition detailed in Table 1.

Material characterization

X-ray diffraction (XRD) was utilized for phase identification and quantification of the as-synthesized amorphous LOTC powder. Crystalline Si powder was mixed with the as-synthesized LOTC powder in a 1:1 weight ratio to serve as the internal standard for phase identification and quantification. The Si + LOTC powder mixture was mixed uniformly through grinding in an agate mortar until a homogeneous color was achieved. The XRD patterns were collected using a Bruker D2 PHASER diffractometer in Bragg-Brentano geometry, employing a Ni-filtered Cu *Kα* radiation (1.5405 Å) and a LynxEye linear position sensitive detector with a step width of 0.01° 2θ and a counting time of 3.5 s/step. To avoid reactions with moisture during the XRD data collection, sample powder was sealed with a Kapton tape. The phase quantification involved comparing the integrated intensities of the diffraction peaks of the phases in the sample to those of the Si reference material. The quantities of the amorphous and crystalline phases are estimated by[32]

$$W_i = \left[K_{iref}\left(\frac{I_i}{I_{ref}} \times W_{ref}\right) \times \frac{1}{W_{tot}}\right] \times 100\% \quad (1)$$

$$W_{amorphous} = 100 - \sum_{i=1}^{n} Corr(W_i) \quad (2)$$

Table 1. Summary of ball milling conditions and ionic conductivity of various samples

Sample ID	Ball milling conditions	Total conductivity (S/cm)	Unknown crystalline phase(s) (%)	Amorphous phase (%)	Crystalline LiCl (%)
7	SS balls for 1 h	7.17×10^{-3}	4.38	88.89	6.73
8	SS balls for 1 h + 15 min	8.30×10^{-3}	0.00	92.82	7.18
5	SS balls for 1 h + 30 min	6.94×10^{-3}	5.68	84.12	10.20
6	SS balls for 1 h + 60 min	5.63×10^{-3}	2.13	83.06	14.81
4	SS balls for 1 h + 120 min	3.54×10^{-3}	3.06	81.67	15.27
9	ZrO_2 balls for 1 h + 15 min	0.063×10^{-3}	5.03	85.37	9.60
1	ZrO_2 balls for 10 h	0.19×10^{-3}	2.20	76.72	21.08

where W_i is the weight percentage of phase i, W_{ref} indicates the weight of the reference in the sample, W_{tot} denotes the total weight of the sample, I_i stands for the integrated intensity of the diffraction peaks for phase i in the sample, I_{ref} represents the integrated intensity of the diffraction peak of the reference material, and $\Sigma_{i=1}^{n} Corr(W_i)$ points to the total percentage of all crystalline phases in the sample. Further, K_{iref}, the reference intensity ratio for phase i, can be determined by creating the known mixture of standard and analyte phases. The known amounts of LiCl and Si were used to determine K_{iref}, assuming it to be the same for the unknown phase(s). Spline interpolation was applied to remove the background from the XRD data.

DSC analysis was conducted using the Setsys 16/18 DTA/DSC from Setaram to determine the stored enthalpy in the amorphous phase and the crystallization temperatures if present. The DSC analyses were performed from 30 °C to 300 °C inside an aluminum crucible covered with a lid under a flowing argon atmosphere with a heating and cooling rate of 5 °C/min.

Electrochemical measurement

First, 200~300 mg of LOTC powder was cold pressed at 200 MPa and then heated to 100 °C to form a pellet in a steel die with a garolite sleeve. The impedance of the pellet with a setup of SS/LOTC/SS was measured via electrochemical impedance spectroscopy (EIS, Gamry INTERFACE 1010E) over a frequency range of 1 Hz - 2 MHz with an applied AC perturbation signal of 30 mV. EIS data analysis and equivalent circuit fitting were performed using Gamry Echem Analyst, and the electrical conductivity of the electrolyte was computed using[33]

$$\sigma = L/RA \tag{3}$$

where σ is the conductivity, L is the thickness of the pellet, R is the resistance and A is the area of the pellet. DC polarization was conducted with a voltage of 5 V right after the EIS measurement. The cyclic voltammetry (CV) was conducted using Gamry INTERFACE 1010E with a semi-blocking cell having a SS/SSE/Li chip/SS (SS/SSE/Li/SS) setup to obtain the electrochemical window. The test was performed at RT with a scanning rate of 1 mV/s within the range of -0.5 V to 6.0 V (*vs.* Li^+/Li).

RESULTS AND DISCUSSION

Materials characterization of ball milled products

The XRD patterns of various samples are summarized in Figure 1 which has arranged the XRD patterns of samples with gradually increased ball milling time from the top to the bottom except for the very last sample

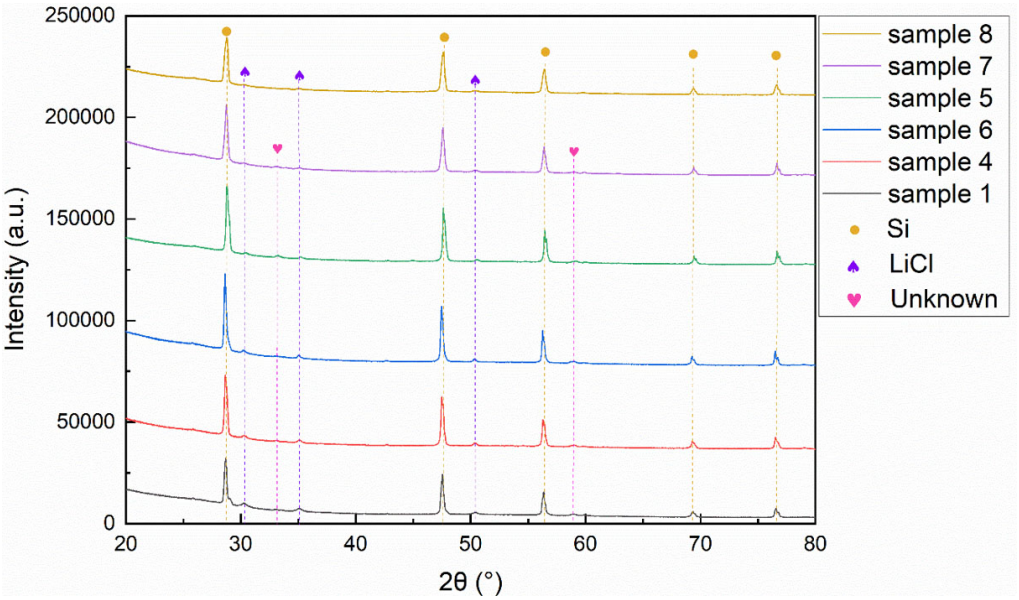

Figure 1. XRD patterns of various ball milled samples as a function of ball milling conditions. See Table 1 for the details of ball milling conditions. XRD: X-ray diffraction.

ball milled using ZrO_2 balls. Several trends are noted. First, all samples contain a small amount of crystalline LiCl byproduct. Second, all samples have a significant amount of amorphous phase. Third, some samples (e.g., samples 1, 4, 5, 6 and 7) also have unknown crystalline phase(s). By comparing the integrated intensities of the diffraction peaks of the phases in the sample to those of the Si internal reference and utilization of Eqs. (1) and (2), the quantities of crystalline LiCl byproduct along with the amorphous phase and unknown crystalline phase(s) in all samples have been estimated and summarized in Table 1. A close examination of Table 1 reveals that the quantity of each phase is a function of the ball milling time and the balls used. Specifically, sample 7 with 1-h ball milling time has the lowest LiCl content among all samples and the LiCl content increases gradually when the ball milling time increases. In contrast, the quantities of the unknown crystalline phase(s) do not show such a clear dependance on the ball milling time. In addition, sample 8 with 1 h + 15 min ball milling time has the highest quantity of the amorphous phase among all samples.

The seemingly complex trends of the quantities of the amorphous LOTC phase and crystalline LiCl as a function of the ball milling time could be rationalized based on the nature of high-energy ball milling. It is well known that high-energy ball milling carried out using SPEX, attritor and planetary mills leads to repeated deformation, fracture and cold-welding of particles, introduction of structural defects (such as vacancies, dislocations and grain boundaries) into crystalline materials, the formation of an amorphous phase, and even the formation of new compounds via in-situ reactions between the reactants[34-40]. Furthermore, after the formation of an amorphous phase, a crystalline phase can form *in situ* during high-energy ball milling through crystallization of the amorphous phase[39]. In particular, the following two studies are very helpful in understanding the results of the present study. Specifically, a previous study on high-energy ball milling of Si + graphite mixture reveals that crystalline and amorphous SiC can be formed through *in-situ* reactions during ball milling, depending on the ball milling conditions[40]. A different study on high-energy ball milling of anatase-TiO_2 shows that after a sufficient ball milling time amorphous TiO_2 can be formed and further ball milling can result in crystallization of the *in-situ* formed amorphous TiO_2 to become crystalline rutile-TiO_2[39].

Based on the mechanisms established in the previous studies[34-40], synthesis of amorphous LOTC electrolyte through *in-situ* solid-state reactions between Li_2O and $TaCl_5$ enhanced by high-energy ball milling can be envisioned as a result of several simplified processes. These include (i) particle size reduction of Li_2O and $TaCl_5$ powders, (ii) introduction of internal strains and various structural defects into Li_2O and $TaCl_5$ powders, (iii) chemical reaction of Li_2O with $TaCl_5$ to form amorphous LOTC compound, and (iv) formation of crystalline LiCl through decomposition and crystallization of some amorphous LOTC compound. Process (iii) is expected to be enhanced by processes (i) and (ii) through the mechanisms of high reaction interface areas and short diffusion paths maintained dynamically by repeated fracture and coalescence of Li_2O and $TaCl_5$ powder particles, whereas process (iv) is likely due to the temperature rise at the ball collision site which can be as high as 180 °C[38], 325 °C[39], 350 °C[35], and 500 °C[34], depending on the ball milling conditions and powder properties. Based on the proposed simplified processes, several statements can be made. First, 1-h ball milling with SS balls of 5 mm diameter and a charge ratio of 20:1 is sufficient to convert crystalline Li_2O + $TaCl_5$ mixture to an amorphous phase with formation of 6.73 wt% crystalline LiCl and a small amount of unknown crystalline phase(s). Second, when the ball milling time increases to 1 h and 15 min, more amorphous phase is formed with formation of 7.18 wt% crystalline LiCl. Third, as the ball milling time increases beyond 1 h and 15 min, the quantity of the amorphous phase starts to decrease because decomposition and crystallization of the amorphous phase to form crystalline LiCl become dominant processes. Since the nature of the unknown crystalline phase(s) is unclear at this stage, it is not appropriate to make comments on the nature of amorphization of the unknown crystalline phase(s).

It is interesting to note that sample 9 using ZrO_2 balls with 1 h + 15 min ball milling time has less amorphous phase than sample 8 which also has 1 h + 15 min ball milling time but uses SS balls. The lower quantity of the amorphous phase in sample 9 can be attributed to the lower density of ZrO_2 balls (5.68 g/cm^3) than SS balls (~7.8 g/cm^3). Lower density balls have lower kinetic energies and thus lower impact energies during ball milling, leading to slower generation of structural defects and formation of an amorphous phase. When the ball milling time is increased to 10 hours in using ZrO_2 balls (sample 1), the quantity of the amorphous phase decreases from 85.37% for 1-h + 15-min ball milling time to 76.72% for 10-h ball milling time. This pattern is the same as the one using SS balls; i.e., the quantity of the amorphous phase decreases because decomposition and crystallization of the amorphous phase to form crystalline LiCl become dominant processes after long ball milling time.

Electrochemical properties of ball milled products

The impedances of all as-synthesized LOTC powders were determined using EIS. The Nyquist plots for samples 1, 6 and 8 are shown in Figure 2. The Nyquist plots of samples 4, 5 and 7 are similar to those of samples 6 and 8, as shown in Supplementary Figure 1 to avoid crowdedness of Figure 2. It is clear that sample 1 has an incomplete semicircle at the high and intermediate frequency range, followed by a straight line at the low-frequency region. An equivalent circuit, R[Q(QR)]W shown in Figure 2, is used to fit the impedance spectrum of sample 1. It is known that the intercept of the semicircle with the real axis at the highest frequency typically represents the bulk resistance R_{bulk} derived from the resistance to Li-ion transport inside solid electrolyte particles, whereas R_{gb} determined from the semicircle is normally attributed to the resistance of Li-ion diffusion via grain boundaries and/or particle interfaces[33,41,42]. Given that sample 1 is mainly composed of an amorphous phase, the value of R_{bulk} is assigned to the resistance to Li-ion transport inside the amorphous phase, whereas R_{gb} is attributed to the resistance of Li-ion diffusion via the interface of the amorphous phase. The result from the equivalent circuit fitting reveals that the bulk conductivity of the amorphous phase s_{bulk} and the conductivity at the interface s_{gb} are 3.17×10^{-4} and 4.79×10^{-4} S/cm, respectively, indicating that the electrical conductivities within the amorphous phase and at the interface of the amorphous phase are similar. It is known that when the bulk conductivity and the interface conductivity are high, the semicircle at the high and intermediate frequencies typically

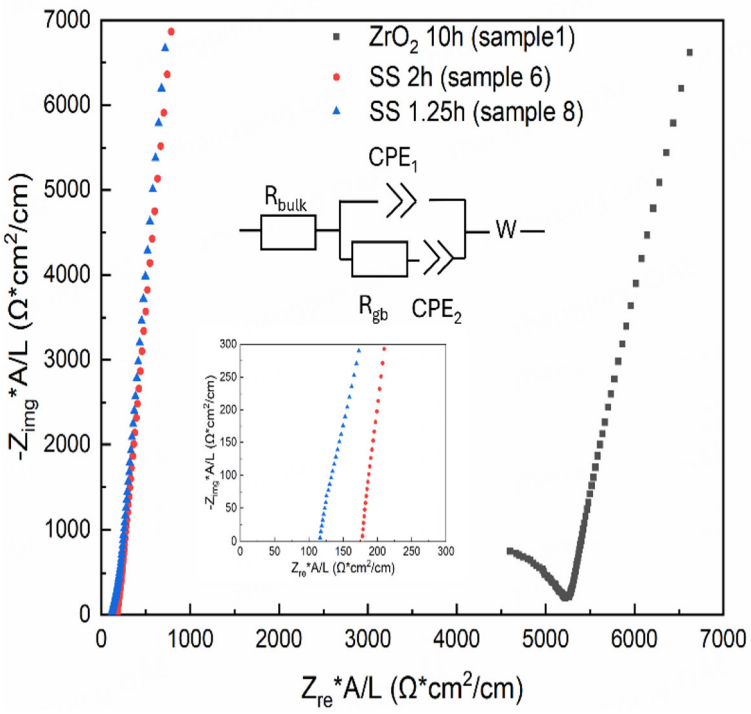

Figure 2. EIS curves of samples 1, 6 and 8. The insert shows the enlarged portion of samples 6 and 8 at the high-frequency range. The equivalent circuit used for curve fitting of sample 1 is provided as well. EIS: Electrochemical impedance spectroscopy.

disappears[41,42]. This is the case for samples 4-8. Under this condition, the bulk conductivity and interface conductivity cannot be separated easily and their combined conductivity is termed as the total conductivity, s_{total}, in this study, as listed in Table 1.

In order to understand the influence of crystalline LiCl on the s_{total} of LOTC samples, pure crystalline LiCl powder was pressed into pellets under 200 MPa at 100 °C and subsequently their conductivities were measured using EIS at 100 °C and RT. The Nyquist plots of crystalline LiCl at 100 °C and RT are shown in Supplementary Figure 2A and B, respectively. It is found that R[Q(QR)]W equivalent circuits fit their EIS curves well, revealing that the s_{total} of crystalline LiCl s_{total} is ~1.52×10^{-7} S/cm at 100 °C. At RT, the s_{total} drops substantially to 5.89×10^{-10} S/cm. These results unambiguously reveal that the s_{total} of crystalline LiCl at RT is seven orders of magnitude lower than that of LOTC samples. Therefore, it can be concluded that the presence of crystalline LiCl inside LOTC samples is detrimental to the s_{total} of LOTC samples. This conclusion is consistent with the data listed in Table 1 based on which the s_{total} of LOTC samples as a function of the crystalline LiCl quantity is shown in Figure 3A which reveals a clear trend: increasing the quantity of crystalline LiCl leads to lower s_{total} of LOTC samples.

To find out how other phases affect the conductivity of LOTC samples, the s_{total} of LOTC samples as a function of the amorphous phase quantity, the unknown crystalline phase quantity, and the quantity of the crystalline LiCl plus the unknown crystalline phase are plotted in Figure 3B, Supplementary Figures 3 and 4, respectively. A general trend of increasing the quantity of the amorphous phase leading to enhancement in the s_{total} of LOTC samples is observed in Figure 3B. More importantly, sample 8 has the highest quantity of the amorphous phase and the highest ionic conductivity in spite of its higher LiCl content than that of sample 7. These trends unambiguously reveal that it is the amorphous phase that provides high ionic conductivity to LOTC samples. No clear trends are observed for the quantity of the unknown crystalline

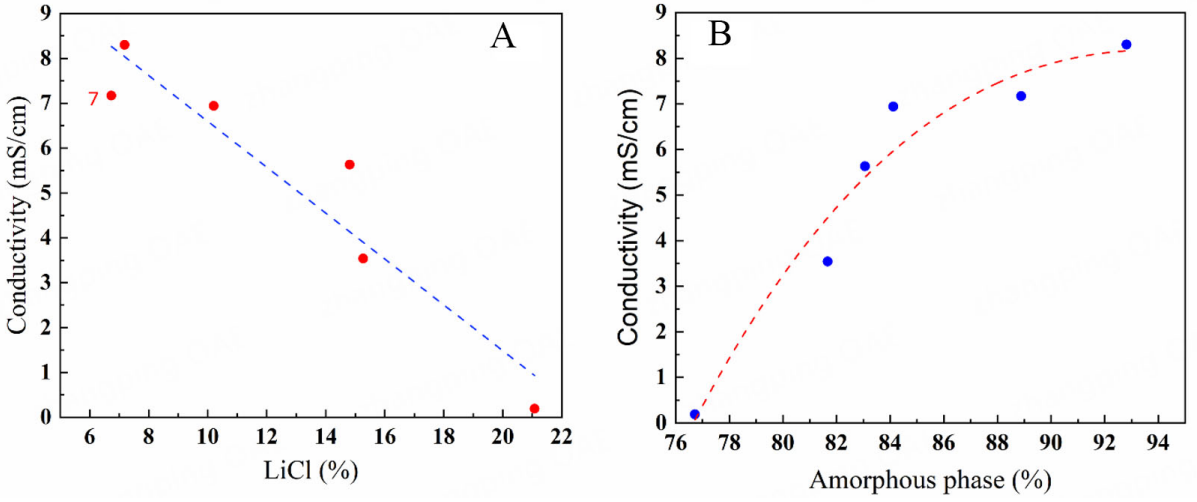

Figure 3. (A) The total conductivity of LOTC samples as a function of the quantity of crystalline LiCl phase; and (B) the total conductivity of LOTC samples as a function of the amorphous phase quantity, showing two clear trends: (i) decreasing the total conductivity with increasing the crystalline LiCl and (ii) increasing the total conductivity with increasing the amorphous phase. The dashed lines serve as a guide for the eyes only. LOTC: $1.6Li_2O$-$TaCl_5$.

phase [Supplementary Figure 3]. Taking all the data in Table 1, Figures 2 and 3, and Supplementary Figures 1-4 together, it can be concluded that (i) it is the amorphous phase that offers high ionic conductivity to LOTC samples, (ii) crystalline LiCl is detrimental to the s_{total} of LOTC samples, and (iii) the effects of the unknown crystalline phase(s) on the s_{total} of LOTC samples are small.

To separate the electronic and ionic conductivities, DC polarization experiments were conducted with the application of a 5 V voltage [Figure 4A and Supplementary Figure 5]. The electronic conductivity of sample 8, which has the highest s_{total}, is determined at 4,000 s of the Direct current (DC) polarization experiment and found to be 2.46×10^{-9} S/cm which is significantly lower than its s_{total} (8.30×10^{-3} S/cm). The electronic conductivity of sample 1, which has the lowest s_{total} (0.19×10^{-3} S/cm) in this study, is found to be 1.81×10^{-9} S/cm [Supplementary Figure 5]. As such, the electrical conductivities of LOTC samples are mainly dictated by the ionic conductivity, and therefore, LOTC powder is suitable for applications as a SSE from the conductivity viewpoint.

CV analysis is conducted at RT with a scanning rate of 1 mV/s within the range of -0.5 V to 6.0 V *vs.* Li^+/Li. The scan starts at 0.0 V, increases to 6.0 V, and then decreases to -0.5 V *vs.* Li^+/Li [Figure 4B]. It is noted that there is an oxidation peak at ~2.3 V and a reduction peak at ~1.3 V, but sample 8 is stable against oxidation between 2.3 V and 6.0 V (the upper limit of our device). The CV scan starting at the open circuit voltage (OCV=1.99 V) is also measured [Supplementary Figure 6]. The conclusion obtained is the same as that obtained from the CV measurement starting from 0 V [Figure 4B]. Thus, LOTC electrolytes have the potential to be used as an electrolyte for many cathode materials including 5 V cathodes (such as $LiNi_{0.5}Mn_{1.5}O_4$ cathode). In fact, Zhang *et al.*[31] have used LOTC solid electrolytes in $LiNi_{0.83}Co_{0.11}Mn_{0.06}O_2$ cathodes, the LOTC/Li_3YCl_6 as a double layer separator, and Li-In alloy as the anode to fabricate solid-state batteries with stable 2,400 cycles at RT, indicating the effectiveness of these electrolytes.

Degree of amorphization and its effects

A scientifically interesting and technologically important question is whether ionic conductivity is affected by the degree of amorphization. The following phenomena appear to indicate that this is indeed the case.

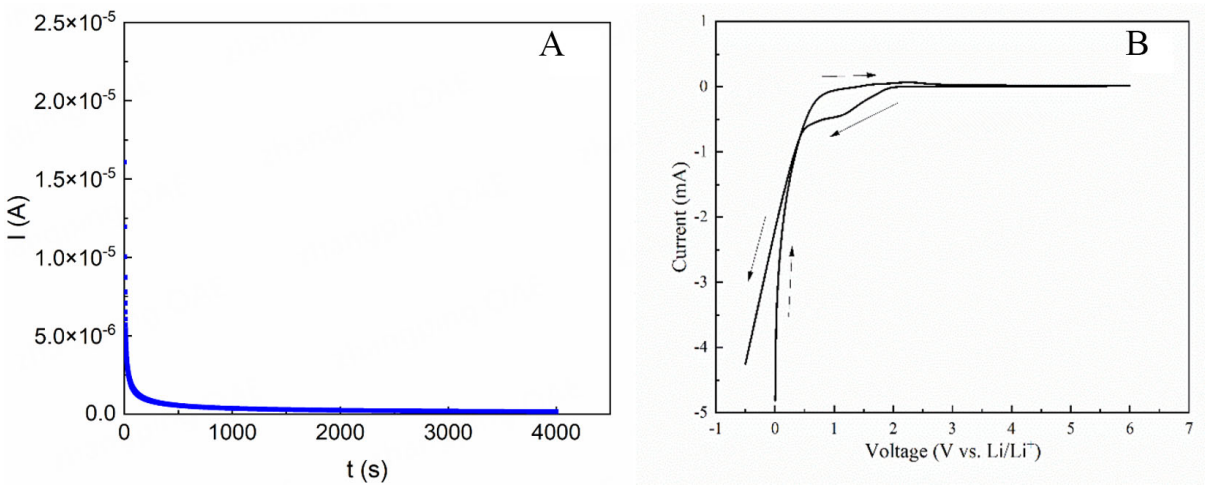

Figure 4. (A) Direct current polarization curve and (B) cyclic voltammetry curve of sample 8 with a semi-blocking cell setup of SS/sample 8/Li/SS, measured at RT. SS: Stainless steel; RT: room temperature.

First, the highest ionic conductivity of LOTC samples obtained in this study (8.3 × 10^{-3} S/cm) is 25% higher than the highest ionic conductivity (6.6 × 10^{-3} S/cm) reported previously[31] even though the chemical compositions of the two studies are the same. Second, there is no linear relationship between the ionic conductivity and the quantity of the amorphous phase [Figure 3B], suggesting that the bulk conductivity of the amorphous phase may change with the nature of the amorphous phase. A direct way to confirm whether this is the case would be to explore the structure of the LOTC amorphous phase that has been studied using Raman spectroscopy, X-ray photoelectron spectroscopy, and X-ray absorption spectroscopy in the previous report[31]. The LOTC amorphous phase has been identified to be composed of two major local structure units, $[TaCl_4O]^-$ and $[TaCl_{5-a}O_a]^{a-}$ ($2 \leq a < 5$), with Li^+ ions mainly interacting with Cl^- ions via unsaturated Ta-Cl···Li bonds[31]. The disordered and irregular $[TaCl_{5-a}O_a]^{a-}$ arrangements in the amorphous LOTC make it possible to form rich Li-Cl interactions and distorted Li-Cl sublattices, while O atoms act as bridges to connect Ta-centered trigonal bipyramids to form the macromolecule network. The unsaturated Ta-Cl···Li bonds in $[TaCl_{5-a}O_a]^{a-}$ have weak Coulombic forces between Li and Cl, making it easier for Li ions to escape from one site and jump to another[31]. If the ionic conductivity of the amorphous LOTC phase changes with the degree of amorphization, then the local structure units and/or their arrangements would have altered as the degree of amorphization changes. This possibility is addressed below through both theoretical arguments and experimental studies.

It is well documented that severe mechanical shear occurs and introduces significant structural defects to powder particles during high-energy ball milling[37,39,40,43]. We postulate that severe mechanical shear can alter the disordered and irregular $[TaCl_{5-a}O_a]^{a-}$ arrangements in amorphous LOTC, leading to more structural defects (such as more Li-ion vacancies and further distortion of Li-Cl sublattices) in the amorphous phase and thus making it easier for Li ions to jump from one site to another with improved ionic conductivities as the degree of amorphization increases. Structural defects stored in the amorphous phase are in a high energy state and provide a driving force for the amorphous phase to change to the structural arrangement with lower structural defects and even to crystalline phases through crystallization. Should such events occur, the energy stored in the amorphous phase will be released, which can be detected via DSC. Therefore, several LOTC samples are analyzed via DSC by heating to 300 °C in an Ar atmosphere with a heating rate of 5 °C/min. As expected, all LOTC samples release some stored enthalpy upon heating to 300 °C [Figure 5]. However, the DSC curves and the quantities of the released enthalpy are different for LOTC samples with

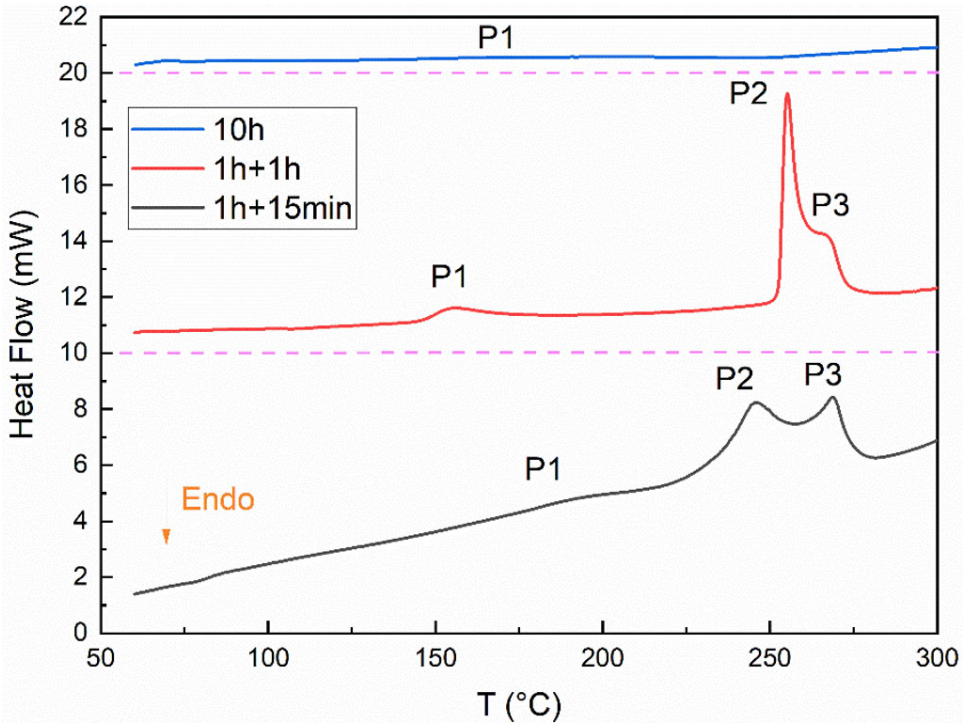

Figure 5. DSC curves of samples 8 (1 h + 15 min ball milling), sample 6 (1 h + 1h ball milling), and sample 1 (10 h ball milling). The exothermic peaks (i.e., release of the stored enthalpy) observed are marked as peak 1 (P1), peak 2 (P2) and peak 3 (P3). The DSC curves of 1 h+1 h and 10 h samples have been offset by 10 mW and 20 mW, respectively, with the dashed lines indicating their respective zero points. DSC: Differential scanning calorimetry.

different ball milling conditions. Specifically, samples 8 and 6 exhibit three exothermic peaks, whereas sample 1 only displays one. Furthermore, peaks 2 (P2) and 3 (P3) for samples 8 and 6 are overlapped and can be separated via curve fitting [Supplementary Figure 7]. The area under each peak normalized by the sample weight represents the quantity of the released enthalpy per gram of the sample for each peak event, and is summarized in Table 2. It can be seen that the quantity of the released enthalpy for each event depends on the sample ball milling conditions, suggesting the complexity of changing the amorphous phase from high energy states to low energy states. Nevertheless, sample 8 releases the largest total enthalpy per milligram of the sample (5.572 mW/mg for P1+P2+P3), followed by sample 6 and then sample 1.

It is noted that the baselines of these samples are different as well. In particular, sample 8 has a positive slope, whereas samples 6 and 1 have a much flat baseline. To find out whether different baselines also reflect energy release processes, the baseline of the DSC machine was determined as well using an empty crucible. As shown in Supplementary Figure 8, the baseline of the DSC machine has a negative slope, suggesting that samples 8, 6 and 1 all gradually release some stored energy during the heating process, but sample 8 has released the most since it has a positive slope as temperature increases from RT to 300 °C. Based on this baseline analysis and Table 2 data, it can be concluded unambiguously that sample 8 has released the largest amount of the stored energy and thus contains the highest defects in its amorphous structures, whereas sample 1 has the lowest defects. This trend is in good accordance with the observed ionic conductivity trend: LOTC samples with higher defects in their amorphous structures have higher ionic conductivities.

To understand the nature of each exothermic peak in the DSC curve, XRD patterns are taken after a sample has been heated passing the peak of interest [Figure 6]. It is found that peak 1 (P1) is associated with

Table 2. Released enthalpy from LOTC samples when heating from RT to 300 °C

Sample ID	P1 (mW/mg)	P2 (mW/mg)	P3 (mW/mg)	Total (P1 + P2 + P3) (mW/mg)
8	0.304	3.754	1.514	5.572
6	0.573	1.553	2.7	4.826
1	0.249	NA	NA	0.249

LOTC: $1.6Li_2O$-$TaCl_5$; RT: room temperature.

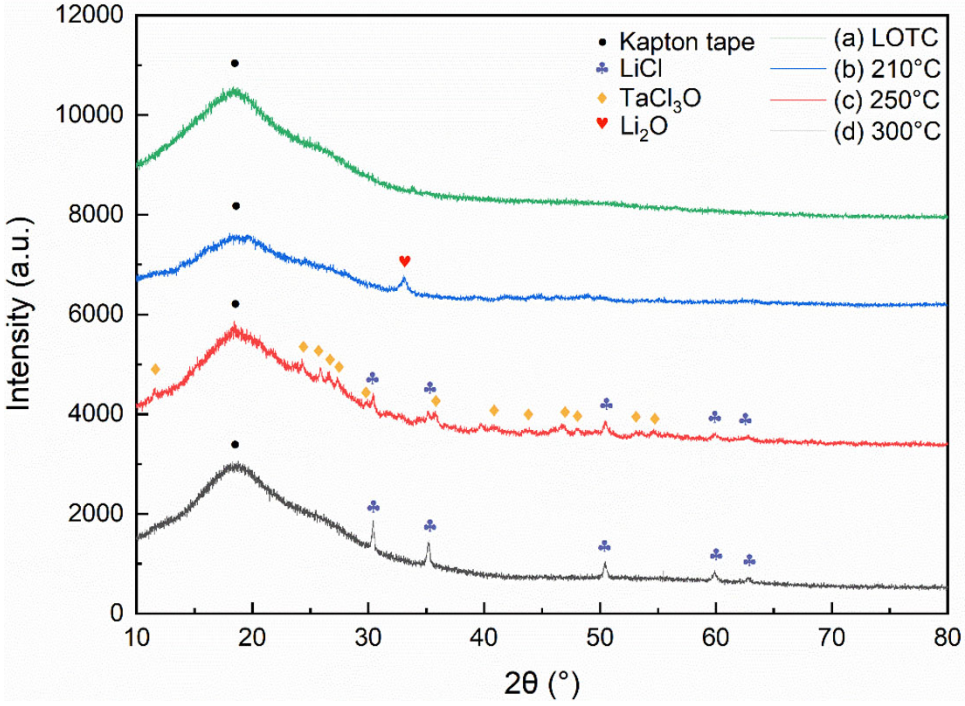

Figure 6. XRD patterns of LOTC sample 8: (a) before DSC heating, (b) after DSC heating to 210 °C, (c) after DSC heating to 250 °C, and (d) after DSC heating to 300 °C. LOTC: $1.6Li_2O$-$TaCl_5$; XRD: X-ray diffraction; DSC: differential scanning calorimetry.

crystallization to form a small quantity of Li_2O phase, whereas peak 2 (P2) is due to the formation of crystalline $TaCl_3O$ with a small amount of crystalline LiCl. Interestingly, at peak 3 (P3) temperature the newly formed crystalline $TaCl_3O$ disappears and a more crystalline LiCl phase is formed. Both samples 8 and 6 exhibit such structural evolution with three exothermic peaks although the onset temperature and peak temperature for these three crystallization events are different for samples 8 and 6. In contrast, sample 1 only exhibits a very broad peak 1 (P1). A possible reason for the absence of peaks 2 and 3 in sample 1 is that it is fabricated via high-energy ball milling using ZrO_2 balls with a very long milling time (10 h), accompanied by the formation of a high concentration of crystalline LiCl phase at the as-synthesized condition [Table 1]. As a result, the high enthalpy of sample 1 induced by high-energy ball milling has been released via in-situ crystallization to form crystalline LiCl during ball milling. These results unequivocally reveal that optimization of high-energy ball milling conditions is essential to achieve the highest structural defects in the amorphous LOTC oxychloride and thus the highest possible ionic conductivity.

Finally, it is worth mentioning that one of the reasons for this study to obtain a higher ionic conductivity than the previous study[31] is the use of SS balls which have a higher density than ZrO_2 balls used in the previous study. As a result, the impact intensity in our study is much higher than that in the previous

study[31], leading to higher degrees of amorphization and higher ionic conductivity as demonstrated in this investigation. Another possible reason for a higher conductivity is the use of SPEX mills in this study. It is known that different ball milling devices such as SPEX, attritor, and planetary mills can lead to varying results in terms of the properties and characteristics of the final products[34,35]. Furthermore, SPEX mills have the highest impact energy among all mills. It is noted that the ball mill machine in the previous study[31] was not reported. Thus, it is not appropriate to discuss this topic further. However, it could be possible that a different type of ball milling machine was used in the previous study[31].

CONCLUSION

A systematic investigation on the formation and ionic conductivity of amorphous LOTC oxychloride has been carried out in this study. Different high-energy ball milling conditions have been applied to create amorphous LOTC oxychlorides with different ionic conductivities and stored enthalpies. Several conclusions can be drawn from this study.

1. The highest ionic conductivity (8.3×10^{-3} S/cm at RT) achieved in this study is obtained using SS balls with 1 h + 15 min milling time beyond which the conductivity starts to decrease. The obtained 8.3×10^{-3} S/cm conductivity is 25% higher than that (6.6×10^{-3} S/cm) reported previously in the literature[31] even though their compositions are identical.

2. The ionic conductivity of ball-milled LOTC is mainly controlled by the quantities of the amorphous phase and crystalline LiCl byproduct in the sample.

3. The reaction byproduct, crystalline LiCl, is harmful to the ionic conductivity because of its very low s_{total}.

4. The quantities of the amorphous phase and crystalline LiCl phase in the LOTC sample depend on the ball milling conditions. Specifically, crystalline LiCl content increases gradually with increasing the milling time.

5. The sample ball milled with ZrO_2 balls has the lowest ionic conductivity because this sample has the highest quantity of crystalline LiCl.

6. DSC analysis reveals that the sample with the highest ionic conductivity releases the highest stored enthalpy upon heating, suggesting that structural defects in amorphous LOTC samples are an important factor for boosting their Li-ion conductivity.

DECLARATIONS

Authors' contributions

Writing - original draft, methodology, investigation, formal analysis, data curation: Ou, J.
Methodology, investigation, formal analysis: Senevirathna, I.
Formal analysis, data curation: Tatagari, V.; Saleem, A.
Writing - review and editing, funding acquisition, formal analysis: Segre, C.
Writing - review and editing, supervision, project administration, investigation, funding acquisition, conceptualization: Shaw, L.

Availability of data and materials

The data that support the findings of this study are available in the Supplementary Materials of this article.

Financial support and sponsorship

This research was financially supported by the U.S. National Science Foundation (NSF) with the award number OISE-2230770. Leon Shaw is also grateful to the Rowe Family Endowment Fund, while Carlo Segre acknowledges the support from the Duchossois Leadership Endowment Fund.

Conflicts of interest

All authors declared that there are no conflicts of interest.

Ethical approval and consent to participate

Not applicable.

Consent for publication

Not applicable.

Copyright

© The Author(s) 2025.

REFERENCES

1. Kong, L.; Li, C.; Jiang, J.; Pecht, M. G. Li-ion battery fire hazards and safety strategies. *Energies* **2018**, *11*, 2191. DOI
2. Schnell, J.; Günther, T.; Knoche, T.; et al. All-solid-state lithium-ion and lithium metal batteries - paving the way to large-scale production. *J. Power. Sources.* **2018**, *382*, 160-75. DOI
3. Zhou, L.; Assoud, A.; Zhang, Q.; Wu, X.; Nazar, L. F. New family of argyrodite thioantimonate lithium superionic conductors. *J. Am. Chem. Soc.* **2019**, *141*, 19002-13. DOI
4. Adeli, P.; Bazak, J. D.; Park, K. H.; et al. Boosting solid-state diffusivity and conductivity in lithium superionic argyrodites by halide substitution. *Angew. Chem. Int. Ed.* **2019**, *58*, 8681-6. DOI
5. Kamaya, N.; Homma, K.; Yamakawa, Y.; et al. A lithium superionic conductor. *Nat. Mater.* **2011**, *10*, 682-6. DOI
6. Kato, Y.; Hori, S.; Saito, T.; et al. High-power all-solid-state batteries using sulfide superionic conductors. *Nat. Energy.* **2016**, *1*, 16030. DOI
7. Sun, Y.; Guan, P.; Liu, Y.; Xu, H.; Li, S.; Chu, D. Recent progress in lithium lanthanum titanate electrolyte towards all solid-state lithium ion secondary battery. *Crit. Rev. Solid. State. Mater. Sci.* **2019**, *44*, 265-82. DOI
8. Lu, J.; Li, Y. Perovskite-type Li-ion solid electrolytes: a review. *J. Mater. Sci. Mater. Electron.* **2021**, *32*, 9736-54. DOI
9. Tao, B.; Ren, C.; Li, H.; et al. Thio-/LISICON and LGPS-type solid electrolytes for all-solid-state lithium-ion batteries. *Adv. Funct. Mater.* **2022**, *32*, 2203551. DOI
10. Kobayashi, T.; Yamada, A.; Kanno, R. Interfacial reactions at electrode/electrolyte boundary in all solid-state lithium battery using inorganic solid electrolyte, thio-LISICON. *Electrochim. Acta.* **2008**, *53*, 5045-50. DOI
11. Li, X.; Liang, J.; Chen, N.; et al. Water-mediated synthesis of a superionic halide solid electrolyte. *Angew. Chem.* **2019**, *131*, 16579-84. DOI
12. Zhou, L.; Kwok, C. Y.; Shyamsunder, A.; Zhang, Q.; Wu, X.; Nazar, L. F. A new halospinel superionic conductor for high-voltage all solid state lithium batteries. *Energy. Environ. Sci.* **2020**, *13*, 2056-63. DOI
13. Liu, X.; Mi, F.; Sun, C. A cost-effective Ca-doped Li_2ZrCl_6 halide solid electrolyte for all-solid-state lithium batteries. *Chem. Commun.* **2025**, *61*, 1144-7. DOI
14. Braga, M. H.; Ferreira, J. A.; Stockhausen, V.; Oliveira, J. E.; El-azab, A. Novel Li_3ClO based glasses with superionic properties for lithium batteries. *J. Mater. Chem. A.* **2014**, *2*, 5470-80. DOI
15. Ou, J.; Tatagari, V.; Senevirathna, I.; et al. On the formation and properties of amorphous and crystalline $Li_{3-y}Ba_{y/2}OCl$ electrolytes. *J. Power. Sources.* **2024**, *609*, 234685. DOI
16. Tanaka, Y.; Ueno, K.; Mizuno, K.; Takeuchi, K.; Asano, T.; Sakai, A. New oxyhalide solid electrolytes with high lithium ionic conductivity >10 mS cm^{-1} for all-solid-state batteries. *Angew. Chem. Int. Ed.* **2023**, *62*, e202217581. DOI PubMed
17. Bates, J.; Dudney, N.; Gruzalski, G.; et al. Fabrication and characterization of amorphous lithium electrolyte thin films and rechargeable thin-film batteries. *J. Power. Sources.* **1993**, *43*, 103-10. DOI
18. Zou, Z.; Xiao, Z.; Lin, Z.; Zhang, B.; Zhang, C.; Wei, F. Lithium phosphorous oxynitride as an advanced solid-state electrolyte to boost high-energy lithium metal battery. *Adv. Funct. Mater.* **2024**, *34*, 2409330. DOI
19. Yin, L.; Yuan, H.; Kong, L.; Lu, Z.; Zhao, Y. Engineering Frenkel defects of anti-perovskite solid-state electrolytes and their applications in all-solid-state lithium-ion batteries. *Chem. Commun.* **2020**, *56*, 1251-4. DOI
20. Majeed, M. K.; Hussain, A.; Hussain, G.; et al. Interfacial engineering of polymer solid-state lithium battery electrolytes and Li-metal anode: current status and future directions. *Small* **2024**, *20*, 2406357. DOI

21. Saleem, A.; Iqbal, R.; Majeed, M. K.; et al. Boosting lithium-ion conductivity of polymer electrolyte by selective introduction of covalent organic frameworks for safe lithium metal batteries. *Nano. Energy.* **2024**, *128*, 109848. DOI
22. Shi, K.; Yu, C.; Zheng, D.; Yang, Z.; Zhang, W. Rational design of continuous and short-range lithium ion pathways based on polydopamine-anchored metal-organic frameworks for all-solid-state electrolytes. *J. Energy. Chem.* **2024**, *99*, 712-24. DOI
23. Tan, J.; Wang, Z.; Cui, J.; et al. Sandwich-type composited solid polymer electrolytes to strengthen the interfacial ionic transportation and bulk conductivity for all-solid-state lithium batteries from room temperature to 120 °C. *J. Energy. Chem.* **2024**, *95*, 288-95. DOI
24. Dai, T.; Wu, S.; Lu, Y.; et al. Inorganic glass electrolytes with polymer-like viscoelasticity. *Nat. Energy.* **2023**, *8*, 1221-8. DOI
25. Hayashi, A.; Hama, S.; Morimoto, H.; Tatsumisago, M.; Minami, T. Preparation of Li_2S-P_2S_5 amorphous solid electrolytes by mechanical milling. *J. Am. Ceram. Soc.* **2001**, *84*, 477-79. DOI
26. Agostini, M.; Aihara, Y.; Yamada, T.; Scrosati, B.; Hassoun, J. A lithium-sulfur battery using a solid, glass-type P_2S_5-Li_2S electrolyte. *Solid. State. Ionics.* **2013**, *244*, 48-51. DOI
27. Wang, Y.; Ouyang, J.; Yuan, H.; et al. Impact of local amorphous environment on the diffusion of sodium ions at the solid electrolyte interface in sodium-ion batteries. *Chin. Chem. Lett.2024*, 110412. DOI
28. Ding, J.; Ji, D.; Yue, Y.; Smedskjaer, M. M. Amorphous materials for lithium-ion and post-lithium-ion batteries. *Small* **2024**, *20*, 2304270. DOI PubMed
29. Ishiguro, Y.; Ueno, K.; Nishimura, S.; Iida, G.; Igarashib, Y. $TaCl_5$-glassified ultrafast lithium ion-conductive halide electrolytes for high-performance all-solid-state lithium batteries. *Chem. Lett.* **2023**, *52*, 237-41. DOI
30. Li, F.; Cheng, X.; Lu, G.; et al. Amorphous chloride solid electrolytes with high Li-ion conductivity for stable cycling of all-solid-state high-nickel cathodes. *J. Am. Chem. Soc.* **2023**, *145*, 27774-87. DOI
31. Zhang, S.; Zhao, F.; Chen, J.; et al. A family of oxychloride amorphous solid electrolytes for long-cycling all-solid-state lithium batteries. *Nat. Commun.* **2023**, *14*, 3780. DOI PubMed PMC
32. Dinnebier, R. E.; Billinge, S. J. *Powder diffraction: theory and practice,* Royal society of chemistry: 2015. https://books.google.com/books?id=wmQ_lFIMkFYC&printsec=frontcover&source=gbs_ge_summary_r&cad=0#v=onepage&q&f=false (accessed 2025-04-22).
33. Luo, M.; Ortiz, A. L.; Shaw, L. L. Unraveling processing-structure-electrical conductivity relationships of $NaCrO_2$ cathodes for Na-ion batteries. *J. Electrochem. Soc.* **2019**, *166*, A3546. DOI
34. Schwarz, R. B.; Koch, C. C. Formation of amorphous alloys by the mechanical alloying of crystalline powders of pure metals and powders of intermetallics. *Appl. Phys. Lett.* **1986**, *49*, 146-8. DOI
35. Davis, R. M.; Mcdermott, B.; Koch, C. C. Mechanical alloying of brittle materials. *Metall. Trans. A.* **1988**, *19*, 2867-74. DOI
36. Shaw, L. L.; Yang, Z.; Ren, R. Mechanically enhanced reactivity of silicon for the formation of silicon nitride composites. *J. Am. Ceram. Soc.* **1998**, *81*, 760-4. DOI
37. Benjamin, J. S.; Volin, T. E. The mechanism of mechanical alloying. *Metall. Trans.* **1974**, *5*, 1929-34. DOI
38. Schaffer, G. B.; Mccormick, P. G. On the kinetics of mechanical alloying. *Metall. Trans. A.* **1992**, *23*, 1285-90. DOI
39. Ren, R.; Yang, Z.; Shaw, L. Polymorphic transformation and powder characteristics of TiO_2 during high energy milling. *J. Mater. Sci.* **2000**, *35*, 6015-26. DOI
40. Yang, Z.; Shaw, L. Synthesis of nanocrystalline SiC at ambient temperature through high energy reaction milling. *Nanostruct. Mater.* **1996**, *7*, 873-86. DOI
41. Jolley, A. G.; Cohn, G.; Hitz, G. T.; Wachsman, E. D. Improving the ionic conductivity of NASICON through aliovalent cation substitution of $Na_3Zr_2Si_2PO_{12}$. *Ionics* **2015**, *21*, 3031-8. DOI
42. Chiang, S.; Kaduk, J. A.; Shaw, L. L. High ionic conducting NaSICON enabled by mechanical activation enhanced reaction. *Mater. Chem. Phys.* **2024**, *312*, 128656. DOI
43. Shaw, L.; Xie, X.; Ren, R.; Yang, Z. NMR studies on mixing of insoluble constituents during high energy milling. *Scr. Mater.* **1998**, *39*, 1169-75. DOI